Synthesis of >20 μm 2D Layered Transition Metal (Ni, Co) Hydroxides via Edge-on Condensation

Lu Ping[1*], Gillian E. Minarik[2*], Hongze Gao[2], Jun Cao[2], Tianshu Li[1], Hikari Kitadai[2], Xi Ling[1,2,3†]

[1] Division of Materials Science and Engineering, Boston University, 15 St. Mary's Street, Boston, MA 02215, USA.

[2] Department of Chemistry, Boston University, 590 Commonwealth Avenue, Boston, MA 02215, USA.

[3] The Photonics Center, Boston University, 8 St. Mary's Street, Boston, MA 02215, USA.

*These authors contributed equally to this work.

[†]Corresponding author. Email: xiling@bu.edu

ABSTRACT

Layered transition metal hydroxides (LTMHs) with transition metal centers sandwiched between layers of coordinating hydroxide anions have attracted considerable interest for their potential in developing clean energy sources and storage technologies. However, two-dimensional (2D) LTMHs remain largely understudied in terms of physical properties and applications in electronic devices. Here, for the first time we report >20 μm α-$Ni(OH)_2$ 2D crystals, synthesized from hydrothermal reaction. And an edge-on condensation mechanism assisted with the crystal field geometry is proposed to understand the 2D intra-planar growth of the crystals, which is also testified through series of systematic comparative studies. We also report the successful synthesis of 2D $Co(OH)_2$ crystals (>40 μm) with more irregular shape due to the slightly distorted octahedral geometry of the crystal field. Moreover, the detailed structural characterization of synthesized α-$Ni(OH)_2$ are performed. The optical band gap energy is extrapolated as 2.54 eV from optical absorption measurements and is measured as 2.52 eV from reflected electrons energy loss spectroscopy (REELS). We further demonstrate its potential as insulating 2D dielectric material for electronic devices. The successful realization of the 2D LTMHs opens the door for future exploration of more fundamental physical properties and device applications.

Keywords: 2D materials; nickel hydroxide; cobalt hydroxide; hydrothermal reaction; 2D crystal grow mechanism.

INTRODUCTION

The first successful exfoliation of graphene in 2004 sparked a dramatic increase in two-dimensional (2D) materials research and the repertoire of reported 2D materials family has since expanded. 2D crystals composed of single- or few-layers of atoms display extraordinary chemical, optical, and electronic properties compared with their bulk 3D counterparts due to quantum confinement effect.[1] Nevertheless, only several 2D materials such as graphene,[2] transition metal dichalcogenides,[3,4] and hexagonal boron nitride,[5] are reasonably well-studied for electronic and optoelectronic applications, thanks to the development of successful synthesis methods for large domains and films. Among the over thousands of van der Waals 2D materials,[6,7] unfortunately, many of them are underexplored experimentally, due to the lack of proper synthesis methods for sufficiently large domains. For example, layered transition metal hydroxides (LTMHs) are a group of materials with van der Waals layered structures, but not well studied as 2D electronic materials so far. Several synthetic methods have been proposed to achieve 2D LTMHs crystals including chemical precipitation,[8–11] electrochemical precipitation,[12,13] chemical aging,[14–16] sol-gel,[17] hydrothermal,[18–21] solvothermal methods,[22] and top-down exfoliations[23]. The obtained materials have demonstrated great capability as high-performance electrocatalysts for oxygen evolution reaction (OER)[24,25] and high-capacity electrode materials for supercapacitors,[26,27] thereby exhibiting great potential for applications in terms of clean energy[28–30] and energy storage.[31–34] However, the reported 2D LTMHs are usually nanosheets,[17,23] nanoplates,[20,35] nanoflowers[36] with domain size from hundreds of nm to a few μm. Larger lateral domains of 2D LTMHs (>10 μm) that are desired for certain applications such as semiconductor devices have never been reported.[37,38] Thus, studies of their electronic and magnetic properties have been limited to theoretical investigation.[39–41]

In this work, we achieve largest ever reported 2D α-$Ni(OH)_2$ single crystals (>20 μm) and $Co(OH)_2$ (>40 μm) in a hydrothermal synthesis process. The 2D growth mechanism of LTMHs is established and its different exertion on different transition metals (Ni, Co) is discussed and explained by spin-state geometry theory. Specifically, $[Ni(H_2O)_6]^{2+}$ that has perfect O_h symmetry, allows the new units adding on via the edge and limits the expansion of the crystals in two directions only. Additionally, a comprehensive experimental study is performed using the hydrothermal method to testify the 2D growth mechanism of LTMHs. Further characterizations on the structure and dielectric properties of the as synthesized 2D $Ni(OH)_2$ reveal high crystallinity, mostly α phase, and bandgap of 2.5 eV with a high dielectric strength of 3.2 MV/cm on a 4.9 nm thick flake, showing a great potential as gate dielectric materials for 2D field effect transistors (FETs) devices. We anticipate this achievement will pave the way for the study of fundamental properties and applications of 2D LTMHs crystals in 2D micro-nanoelectronics devices, which is not accessible on reported LTMH samples with limited domain sizes.

RESULTS AND DISCUSSION

Synthesis and Morphology Characterization of 2D $Ni(OH)_2$ and $Co(OH)_2$

Fig. 1A-B show the crystal structure of α-$M(OH)_2$ (M=Ni and Co), which is a typical layered material with a "sandwich" structure of bivalent metals between two layers of octahedrally-coordinated OH^- anions. The intercalation of H_2O between the layers expands the interlayer distance and distinguishes α phase from β phase, which has a smaller interlayer gap due to the absence of intercalation (Fig. S1). In a typical synthesis condition (more details in Supplementary Information Section 1), we perform the reaction at 120 °C with a cooling rate of 1.5 °C/min, which gives the most and largest 2D domains of $Ni(OH)_2$ (Fig. 1C). The surface morphology is further characterized using scanning electron microscopy (SEM) (Fig. 1C inset),

showing the flakes are continuous and smooth, despite small dis-uniformity probably due to thickness change or contaminations. Moreover, Fig. 1D shows the atomic force microscopy (AFM) image of a flake of 6.3 nm, corresponding to ~8 atomic layers.[42] The average domain size and thickness is 20 μm (Fig. 1E) and 16 nm (Fig. 1F), respectively, through surveying 100 flakes in randomly chosen areas. Notably, this is the largest domain size of 2D $Ni(OH)_2$ ever reported, which is also extraordinary compared to other 2D nanosheets typically synthesized using hydrothermal methods.[19,43–46] We also obtain the aspect ratio (dimensionless) by measuring the diameters of each flake along the two perpendicular directions. The plotted distribution (Fig. 1E inset) indicates about 50% of flakes have an aspect ratio of 1.0 and 84% of surveyed flakes maintain quasi-circular dimensions with aspect ratios within the range of 0.8-1.2. The (quasi-) circular shape observed visually is the consequence of the isotropic and outward radial crystal growth. Specifically, Ni^{2+} with its d^8 configuration (Fig. S2) has an even number of electrons on degenerate orbitals, experiencing no distortion from Jahn-Teller (JT) theorem, which describes spontaneous symmetry breaking to provide energetic stabilization of transition metal complexes when there is an odd number of electrons occupying degenerate orbitals.[47–49] The perfect O_h symmetry on $[Ni(H_2O)_6]^{2+}$ with identical bond length and electron density on all six Ni-H_2O metal-ligand coordination bonds allows the formation of 2D crystals with large domain.

Using similar synthesis conditions, we also successfully obtain $Co(OH)_2$ thin flakes with even larger domains (>40 μm), but the shapes are random rather than circular and the density of such large domains is significantly lower than that of $Ni(OH)_2$ (Fig. 1G). This is also the largest $Co(OH)_2$ ultrathin domains ever reported.[50–52] The surface morphology revealed by SEM (Fig. 1G inset) suggests the continuity of these crystals and shows the edge of $Co(OH)_2$ is less tide compared with $Ni(OH)_2$, which is caused by the high spin d^7 configuration of $[Co(H_2O)_6]^{2+}$. For $[Co(H_2O)_6]^{2+}$ (Fig. S3), it suffers slight JT distortion and has a weak

compression along the *z*-axis due to one vacancy in t_{2g} set, leading to D_{4h} symmetry.[53] The small degree of JT distortions leads to less perfect structural alignment when $[Co(H_2O)_6]^{2+}$ units add onto the exiting seed crystals, which would result in distorted-quasi circular morphology, but the large domain size could still possibly be achieved (Fig. 1G). Another case of JT distortion is presented with $[Cu(H_2O)_6]^{2+}$ (Fig. S4), where the high spin d^9 configuration of Cu^{2+} leads to three electrons in the e_g set, and thus largely elongates along the *z*-axis.[53,54] While the elongated axial bonds in $[Cu(H_2O)_6]^{2+}$ also give the complex D_{4h} symmetry, the degree of distortion is more pronounced owing to the fact that the e_g set are anti-bonding orbitals (Fig. S4A), which would likely to direct the growth on a singular direction (Fig. S4B), forming nanorods[55] or nanobelt[56].

Investigation of the 2D Growth Mechanism of $Ni(OH)_2$

During the synthesis, seed crystals formed by a few Ni^{2+} ions with edge hydroxyl ions and localized negative charge (Fig. 2A I) initiate the 2D growth.[57] In order for a single crystal to maintain electrical neutrality, the negative charged seed crystal attracts more Ni^{2+} ions to approach (Fig. 2A II). Meanwhile, the "hanging" water of solvated $[Ni(H_2O)_6]^{2+}$ units formed in aqueous solution will be substituted by hydroxyl groups rapidly and chemical bonds will be built between seed crystal and $[Ni(H_2O)_6]^{2+}$ units in the solution since the $[Ni(H_2O)_6]^{2+}$ is a stable yet labile species. Once this association has been established, continued substitution will occur at the newly bound metal ion (Fig. 2A III) until it is pulled down into the crystal structure (Fig. 2A IV). The terminal H_2O ligands further deprotonate to form new hanging hydroxy groups and bind with new approaching $[Ni(H_2O)_6]^{2+}$ units (Fig. 2A V). Since each surface OH^- of seed crystal is already bonded with three Ni^{2+} and have fully incorporated into the crystal structure (Fig. 2A), the free moving $[Ni(H_2O)_6]^{2+}$ units tend to approach these intra-planar "hanging" ligands at the edge that have strong localized negative charge. Thus, the expansion is limited to two dimensions only, leading to the formation of 2D structure.

In order to testify the mechanism, we investigated the influence of several parameters to the synthesis including the temperature, cooling rate and pH. The detailed discussion can be found in Supporting Information (Section 2). Here we focus on the discussion of the role of NH_3 to support the proposed 2D growth mechanism. As a stronger field ligand compared with H_2O, NH_3 could bond with solvated Ni^{2+} and form $[Ni(NH_3)_6]^{2+}$ (Fig. 2B I), competing with $[Ni(H_2O)_6]^{2+}$ at the nuclei edge. However, unlike $[Ni(H_2O)_6]^{2+}$, the addition of $[Ni(NH_3)_6]^{2+}$ onto nuclei will terminate the expansion of 2D crystals since the edge NH_3 hardly can deprotonate to maintain the localized negative charge (Fig. 2B V). Therefore, the resulting crystals would have smaller domain size, which is also observed from our experiment results.

Fig. 2C shows the optical images of the obtained 2D $Ni(OH)_2$ without additional NH_4OH, where numerous 2D circular flakes are observed. And with 0.6 ml additional NH_4OH (Fig. 2D), domain size of the flakes significantly decreases. Optical images of obtained 2D $Ni(OH)_2$ with different amounts of additional NH_4OH can be found in Fig. S5, showing with increasing amount of additional NH_4OH, the domain size decreases and eventually bulk aggregates are yielded instead of 2D crystals. This is due to the hydrolysis of NH_4OH, which brings more NH_3 into the system to form more $[Ni(NH_3)_6]^{2+}$ or monohydrate substituted $[Ni(H_2O)_x(NH_3)_{6-x}]^{2+}$ (where $x\geq1$), which prevents the 2D expansion based on our proposed mechanism described above. This hypothesis is further supported by the UV-Vis measurements (Fig. 2E). Three absorption bands assigned left to right as $^3A_{2g} \rightarrow {}^3T_{1g}$ (^3F), $^3A_{2g} \rightarrow {}^3T_{1g}$ (^3F), $^3A_{2g} \rightarrow {}^3T_{2g}$, are consistent with homoleptic six-coordinate Ni(II) complexes.[58] The increased absorption intensity (purple curve) and blue color (Fig. 2E inset) with 0.6 ml additional NH_4OH both suggest more $[Ni(H_2O)_x(NH_3)_{6-x}]^{2+}$ are formed.

Structural and Crystallographic Characterization of 2D α-$Ni(OH)_2$

We further characterize the synthesized $Ni(OH)_2$ flakes using XPS. The survey spectrum (Fig. S6A) clearly indicates the presence of Ni and O elements.[59] The core-level spectrum of Ni 2p (Fig. 3A) shows the two major peaks at 856.1 (Ni $2p_{3/2}$) and 873.8 eV (Ni $2p_{1/2}$) with a spin-orbital coupling caused splitting of 17.6 eV, which is characteristic of the Ni^{2+} ion in $Ni(OH)_2$.[60,61] Meanwhile, the O 1s spectrum (Fig. S6B) is fitted with three peaks located at 531.1, 532.4 and 533.2 eV, representing Ni-O-H, O-Si-O and H-O-H, respectively.[62] The appearance of H-O-H signal suggests the existence of H_2O in the crystal, mainly as intercalation species between layers to form α-$Ni(OH)_2$.

To better probe the crystal phase of the 2D thin flakes, surface-enhanced Raman spectroscopy (SERS) measurement using a commercial Ag-nanopillar-coated substrate (Fig. 4B inset) is performed, to boost the weak vibration of 2D thin flakes under conventional Raman. The fingerprint for identifying α-$Ni(OH)_2$ from β-$Ni(OH)_2$ or the mixture is observed at 3610 cm^{-1}(Fig. 4B).[14,63] Moreover, the phonon mode of α-$Ni(OH)_2$ is observed at 460 cm^{-1}, the 2nd order phonon modes of α-$Ni(OH)_2$ are observed at 979 and 1055 cm^{-1}, further proving α phase of the synthesized $Ni(OH)_2$.

More importantly, transmission electron microscopy (TEM) measurements are carried out to further reveal the structure in the flakes. The low-resolution TEM image in Fig. 4C reveals the 2D nature of a micrometer large domain of a typical sample. The selected area electron diffraction (SAED) (Fig. 4C inset) reveals the hexagonal lattice structure, matching well with the simulated lattice pattern (Fig. S7).[64]. The sharp signals from the SAED pattern also suggest the high crystallinity of the sample. Moreover, atomic-resolution TEM image (Fig. 4D) shows the spacing between (301) planes is 1.50 Å. And the 2D α-$Ni(OH)_2$ are stable under high temperature up to 150 °C (Fig. S8A) and in various solvents (Fig. S8B).

Optical and Electric Characterization of 2D α-$Ni(OH)_2$

Ultraviolet–visible spectroscopy (UV-Vis) is carried out on $Ni(OH)_2$ thin flakes spin-coated on indium tin oxide (ITO) coated glass. The optical absorption spectrum (Fig. 4A) is obtained from 300 nm to 700 nm. In addition, two bandgaps are extrapolated from the Tauc plot (Fig. 4B), 2.54 eV and 3.51 eV, corresponding to few-layers[65,66] and bulk $Ni(OH)_2$,[65,66] respectively. Note that the bandgap of 2D α-$Ni(OH)_2$ is smaller than that of its bulk counterpart, which has been reported as an exceptional deviation from the quantum confinement effect[65] and is opposite from most other 2D materials.[67,68] Moreover, the optical bandgap is also measured using reflected electrons energy loss spectroscopy (REELS). As shown in Fig. 4C, a bandgap of 2.52 eV is obtained by measuring the distance between the center of elastic scattering peak and the cutoff of the low energy loss region.

Together with its large domain size, the relatively large bandgap of 2D α-$Ni(OH)_2$ motivates us to investigate its dielectric properties. An Au-$Ni(OH)_2$-Ti sandwich-like structure is fabricated for dielectric property measurements (Fig. 4D), where the top Ti electrode is grounded and voltage is applied on the bottom Au electrodes. Fig. 4E shows the typical I-V curves of the devices (as shown in Fig. 4E inset) based on samples with different thicknesses from 4.9 to 18.3 nm. For all four devices, the current grows exponentially with positive voltage, while a much lower or negligible current is observed with negative voltage. This unipolar conducting characteristic is attributed to the difference in Schottky barrier height (S.B.H.) at the Au-$Ni(OH)_2$ and Ti-$Ni(OH)_2$ interfaces. Given a much higher work function of Au compared to Ti, Au is expected to form a higher barrier with 2D $Ni(OH)_2$.[69] When a positive voltage is applied on the Au electrode, this barrier is forward biased, resulting in an exponential I-V curve once the voltage exceeds its threshold value (Fig. S9A). Otherwise, the barrier is reversely biased, and no current is present before breakdown. We further convert the bias voltage into electric field strength to extract the breakdown field of each device (Fig. 4F), which is 4.47, 2.92, 1.73 and 1.64 MV/cm for 4.9, 8.6, 14.8, and 18.3 nm $Ni(OH)_2$ flakes, respectively

(Fig. S9B). The above breakdown field values are comparable with so far reported dielectric materials (3-12 MV/cm)[70,71] and the reduced dielectric strength at higher thickness is also observed in other 2D dielectric materials (e.g., h-BN)[72]. Nonetheless, all the four tested flakes meet the requirement for gate dielectric layers of field effect transistors (FETs), as the leaking current is below 10 A/cm^2 at a field strength of 2.5 MV/cm.[73] Thus, the addition of $Ni(OH)_2$ to the 2D family provides a promising candidate as dielectric materials for future micro-nanoelectronics devices. From the synthesis point of view, the results demonstrate the great continuity and uniformity of the synthesized 2D $Ni(OH)_2$ flakes.

CONCLUSION

In conclusion, we achieve the largest ever reported 2D $Ni(OH)_2$ (>20 μm) and $Co(OH)_2$ (>40 μm) crystals down to a few nanometers in the hydrothermal synthesis process with a comprehensive understanding of the growth mechanism. Specifically, a direct relationship between spin-state controlled metal-ligand geometry and macroscopic morphology of the LTMHs is built, illustrating the preferred geometry from the growth. A 2D growth mechanism via edge-on condensation at atomic level is established for the hydrothermal synthesis of $Ni(OH)_2$ through a systematic investigation on the influence of key parameters. The reaction-morphology relationship elaborated herein provides a blueprint for a well-guided approach towards the successful design and development of more 2D LTMHs. Moreover, the detailed characterization on the synthesized $Ni(OH)_2$ flakes shows the high crystallinity, α phase, and large bandgap of 2.5 eV. Electrical measurements further suggest the great potential of using $Ni(OH)_2$ as dielectric materials in 2D electronic devices. Considering the great scalability of the hydrothermal synthesis method, our work suggests a promising future of joining LTMHs in the 2D family as a group of important members for future micro-nanoelectronics.

ASSOCIATED CONTENT

Supporting information

The supporting information is provided in a separate document.

Author information

Xi Ling – *Department of Chemistry, Boston University, Boston, Massachusetts 02215, United States; Division of Materials Science and Engineering, Boston University, Boston, Massachusetts 02215, United States; The Photonics Center, Boston University, Boston, Massachusetts 02215, United States;* Email: xiling@bu.edu

Lu Ping – *Division of Materials Science and Engineering, Boston University, Boston, Massachusetts 02215, United States;* Email: luping@bu.edu

Gillian E. Minarik – *Department of Chemistry, Boston University, Boston, Massachusetts 02215, United States;* Email: gminarik@bu.edu

Hongze Gao – *Department of Chemistry, Boston University, Boston, Massachusetts 02215, United States;* Email: rexgao96@bu.edu

Jun Cao – *Department of Chemistry, Boston University, Boston, Massachusetts 02215, United States;* Email: jcao@bu.edu

Tianshu Li – *Division of Materials Science and Engineering, Boston University, Boston, Massachusetts 02215, United States;* Email: tianshul@bu.edu

Hikari Kitadai – *Department of Chemistry, Boston University, Boston, Massachusetts 02215, United States;* Email: hk91@bu.edu

Author contributions

L. P. and X. L. conceived and designed the experiments. L. P., G. M., performed all the synthesis. L. P., H. G., T. L., J. C. and H. K. characterized the samples. L. P., G. M. and X.L. analyzed the data and wrote the manuscript. All authors discussed the results and commented on the manuscript.

Notes

The authors declare no competing interest.

Acknowledgement

Funding: Acknowledgement is made to the donors of the American Chemical Society Petroleum Research Fund for support of this research. X.L. acknowledges the support of Boston University and Boston University Photonics Center. T.L.,J.C. and X.L. acknowledge the support from the U.S. Department of Energy (DOE), Office of Science, Basic Energy Sciences (BES), under Award DE-SC0021064. L.P. and X.L. also acknowledge the support of Ignition Award from Boston University. H.Z.G. acknowledges the support of BUnano Cross-Disciplinary Fellowship. H.K. and X.L. acknowledge the support of the National Science Foundation (NSF) under Grant No. (1945364). **Facility support:** Acknowledgement is made to Prof. Kenneth Burch's group at Boston College for device fabrication assistance; to Harvard Center of Nanoscale System (CNS) for XPS Measurements; to Thermo Fisher Scientific for REELS measurement.

Data Availability: The data that support the findings of this study are available from the corresponding author upon reasonable request.

REFERENCES

[1] J. Tan, S. Li, B. Liu, H.-M. Cheng, *Small Struct.* **2021**, *2*, 2000093.

[2] I. V. G. and A. A. F. K. S. Novoselov, A. K. Geim, S. V. Morozov, D. Jiang, Y. Zhang, S. V. Dubonos, **2016**, *306*, 666.

[3] A. Carvalho, R. M. Ribeiro, A. H. Castro Neto, *Phys. Rev. B - Condens. Matter Mater. Phys.* **2013**, *88*, 1.

[4] A. S. Rodin, L. C. Gomes, A. Carvalho, A. H. Castro Neto, *Phys. Rev. B* **2016**, *93*, 1.

[5] H. Liu, A. T. Neal, Z. Zhu, Z. Luo, X. Xu, D. Tománek, P. D. Ye, *ACS Nano* **2014**, *8*, 4033.

[6] G. Cheon, K. A. N. Duerloo, A. D. Sendek, C. Porter, Y. Chen, E. J. Reed, *Nano Lett.* **2017**, *17*, 1915.

[7] K. S. Novoselov, A. Mishchenko, A. Carvalho, A. H. Castro Neto, *Science (80-.).* **2016**, *353*, DOI 10.1126/science.aac9439.

[8] L. Gourrier, S. Deabate, T. Michel, M. Paillet, P. Hermet, J. L. Bantignies, F. Henn, *J. Phys. Chem. C* **2011**, *115*, 15067.

[9] Y. Wang, D. Cao, G. Wang, S. Wang, J. Wen, J. Yin, *Electrochim. Acta* **2011**, *56*, 8285.

[10] K. Feng, W. Li, S. Xie, X. Lu, *Electrochim. Acta* **2014**, *137*, 108.

[11] J. Camardese, E. McCalla, D. W. Abarbanel, J. R. Dahn, *J. Electrochem. Soc.* **2014**, *161*, A814.

[12] J. Tizfahm, B. Safibonab, M. Aghazadeh, A. Majdabadi, B. Sabour, S. Dalvand, *Colloids Surfaces A Physicochem. Eng. Asp.* **2014**, *443*, 544.

[13] R. S. Jayashree, P. Vishnu Kamath, *J. Appl. Electrochem.* **1999**, *29*, 449.

[14] D. S. Hall, D. J. Lockwood, S. Poirier, C. Bock, B. R. MacDougall, *ACS Appl. Mater. Interfaces* **2014**, *6*, 3141.

[15] M. Osińska, T. Stefanowicz, D. Paukszta, *J. Hazard. Mater.* **2004**, *112*, 177.

[16] C. Tessier, L. Guerlou-Demourgues, C. Faure, M. Basterreix, G. Nabias, C. Delmas, *Solid State Ionics* **2000**, *133*, 11.

[17] H. Cui, J. Xue, W. Ren, M. Wang, *J. Nanoparticle Res.* **2014**, *16*, DOI 10.1007/s11051-014-2601-1.

[18] M. Dixit, G. N. Subbanna, P. V. Kamath, *J. Mater. Chem.* **1996**, *6*, 1429.

[19] L. X. Yang, Y. J. Zhu, H. Tong, Z. H. Liang, L. Li, L. Zhang, *J. Solid State Chem.* **2007**, *180*, 2095.

[20] L. Dong, Y. Chu, W. Sun, *Chem. - A Eur. J.* **2008**, *14*, 5064.

[21] X. Ma, J. Liu, C. Liang, X. Gong, R. Che, *J. Mater. Chem. A* **2014**, *2*, 12692.

[22] M. Wang, Y. Ni, L. Cao, D. Zhao, X. Ma, *J. Colloid Interface Sci.* **2013**, *401*, 8.

[23] A. Harvey, X. He, I. J. Godwin, C. Backes, D. McAteer, N. C. Berner, N. McEvoy, A.

Ferguson, A. Shmeliov, M. E. G. Lyons, V. Nicolosi, G. S. Duesberg, J. F. Donegan, J. N. Coleman, *J. Mater. Chem. A* **2016**, *4*, 11046.

[24] M. Gao, W. Sheng, Z. Zhuang, Q. Fang, S. Gu, J. Jiang, Y. Yan, *J. Am. Chem. Soc.* **2014**, *136*, 7077.

[25] S. Li, Y. Wang, S. Peng, L. Zhang, A. M. Al-Enizi, H. Zhang, X. Sun, G. Zheng, *Adv. Energy Mater.* **2016**, *6*, 1.

[26] W. Sun, X. Rui, M. Ulaganathan, S. Madhavi, Q. Yan, *J. Power Sources* **2015**, *295*, 323.

[27] M. Aghazadeh, S. Dalvand, M. Hosseinifard, *Ceram. Int.* **2014**, *40*, 3485.

[28] J. Yu, Y. Hai, B. Cheng, *J. Phys. Chem. C* **2011**, *115*, 4953.

[29] J. Deng, F. Wu, S. Gao, D. D. Dionysiou, L.-Z. Huang, *Appl. Catal. B Environ.* **2022**, *309*, 121258.

[30] S. J. Patil, N. R. Chodankar, S. K. Hwang, G. S. Rama Raju, Y. S. Huh, Y. K. Han, *Small* **2022**, *18*, DOI 10.1002/smll.202103326.

[31] Z. H. Huang, F. F. Sun, Z. Y. Yuan, W. Sun, B. Jia, H. Li, H. Li, T. Ma, *Nano Energy* **2021**, *82*, 105727.

[32] Y. Wu, H. Chen, Y. Lu, J. Yang, X. Zhu, Y. Zheng, G. Lou, Y. Wu, Q. Wu, Z. Shen, Z. Pan, *J. Colloid Interface Sci.* **2021**, *581*, 455.

[33] H. Chen, L. Hu, M. Chen, Y. Yan, L. Wu, *Adv. Funct. Mater.* **2014**, *24*, 934.

[34] L. Wan, P. Wang, *Int. J. Hydrogen Energy* **2021**, *46*, 8356.

[35] Y. Wang, S. Gai, N. Niu, F. He, P. Yang, *J. Mater. Chem. A* **2013**, *1*, 9083.

[36] H. D. Mai, S. Kim, H. Yoo, *J. Ind. Eng. Chem.* **2020**, *82*, 359.

[37] H. Gao, J. Cao, T. Li, W. Luo, M. Gray, N. Kumar, K. S. Burch, X. Ling, *Chem. Mater.* **2022**, *34*, 351.

[38] J. Cao, T. Li, H. Gao, Y. Lin, X. Wang, H. Wang, T. Palacios, X. Ling, *Sci. Adv.* **2020**, *6*, 1.

[39] Z. Tang, C. Tong, W. Geng, D. Zhang, L. Liu, **2015**, *2*.

[40] Z. K. Tang, W. W. Liu, D. Y. Zhang, W. M. Lau, L. M. Liu, *RSC Adv.* **2015**, *5*, 77154.

[41] X. L. Wei, Z. K. Tang, G. C. Guo, S. Ma, L. M. Liu, *Sci. Rep.* **2015**, *5*, 1.

[42] D. S. Hall, D. J. Lockwood, C. Bock, B. R. MacDougall, *Proc. R. Soc. A Math. Phys. Eng. Sci.* **2015**, *471*, DOI 10.1098/rspa.2014.0792.

[43] M. B. Zaman, R. Poolla, S. A. Khandy, A. Modi, R. K. Tiwari, *Nanotechnology* **2021**, *32*, DOI 10.1088/1361-6528/abec09.

[44] M. Wu, K. Zhu, P. Liang, Z. Yao, F. Shi, J. Zhang, K. Yan, J. Liu, J. Wang, *J. Alloys Compd.* **2021**, *877*, 160174.

[45] H. Liu, Z. Liang, S. Liu, L. Zhang, H. Xia, W. Xie, *Results Phys.* **2020**, *16*, 102831.

[46] Y. feng Deng, Y. Chen, X. li Zhang, Q. Zhang, Z. jian Wei, D. Wang, *J. Alloys*

Compd. **2022**, *892*, 162159.

[47] H.A. Jahn and E. Teller, *Proc. R. Soc. London* **1937**, *161*, 220.

[48] I. B. Bersuker, *Chem. Rev.* **2001**, *101*, 1067.

[49] I. B. Bersuker, *Chem. Rev.* **2021**, *121*, 1463.

[50] J. Li, Z. Li, F. Zhan, M. Shao, *Chem. Sci.* **2021**, *12*, 1756.

[51] A. A. S. Rovetta, M. P. Browne, A. Harvey, I. J. Godwin, J. N. Coleman, M. E. G. Lyons, *Nanotechnology* **2017**, *28*, DOI 10.1088/1361-6528/aa7f1b.

[52] P. Balasubramanian, S. Bin He, H. H. Deng, H. P. Peng, W. Chen, *Sensors Actuators, B Chem.* **2020**, *320*, 128374.

[53] F. A. Cotton, L. M. Daniels, C. A. Murillo, J. F. Quesada, *Inorg. Chem.* **1993**, *32*, 4861.

[54] M. A. Halcrow, *Chem. Soc. Rev.* **2013**, *42*, 1784.

[55] J. Chen, J. Xu, S. Zhou, N. Zhao, C. P. Wong, *J. Mater. Chem. A* **2015**, *3*, 17385.

[56] B. K. Satpathy, S. Patnaik, D. Pradhan, *ACS Appl. Energy Mater.* **2022**, *5*, 77.

[57] G. J. A. A. De Soler-Illia, *Chem. Mater.* **1999**, *11*, 3140.

[58] T. Stankus, *Inorganic Chemistry*, **1996**.

[59] J. Tian, Y. Xue, X. Yu, Y. Pei, H. Zhang, J. Wang, *RSC Adv.* **2019**, *9*, 17706.

[60] X. Cai, X. Shen, L. Ma, Z. Ji, C. Xu, A. Yuan, *Chem. Eng. J.* **2015**, *268*, 251.

[61] F. He, Z. Hu, K. Liu, S. Zhang, H. Liu, S. Sang, *J. Power Sources* **2014**, *267*, 188.

[62] J. R. Rani, R. Thangavel, M. Kim, Y. S. Lee, J. H. Jang, *Nanomaterials* **2020**, *10*, 1.

[63] D. S. Hall, D. J. Lockwood, S. Poirier, C. Bock, B. R. MacDougall, *J. Phys. Chem. A* **2012**, *116*, 6771.

[64] E. Mafakheri, A. H. Tavabi, P. H. Lu, R. Balboni, F. Venturi, C. Menozzi, G. C. Gazzadi, S. Frabboni, A. Sit, R. E. Dunin-Borkowski, E. Karimi, V. Grillo, *Appl. Phys. Lett.* **2017**, *110*, DOI 10.1063/1.4977879.

[65] M. Nagli, M. Caspary Toroker, *J. Chem. Phys.* **2018**, *149*, DOI 10.1063/1.5051202.

[66] A. Pareek, P. Paik, P. H. Borse, *Dalt. Trans.* **2016**, *45*, 11120.

[67] A. Chaves, J. G. Azadani, H. Alsalman, D. R. da Costa, R. Frisenda, A. J. Chaves, S. H. Song, Y. D. Kim, D. He, J. Zhou, A. Castellanos-Gomez, F. M. Peeters, Z. Liu, C. L. Hinkle, S. H. Oh, P. D. Ye, S. J. Koester, Y. H. Lee, P. Avouris, X. Wang, T. Low, *npj 2D Mater. Appl.* **2020**, *4*, DOI 10.1038/s41699-020-00162-4.

[68] T. Jiang, H. Liu, D. Huang, S. Zhang, Y. Li, X. Gong, Y. R. Shen, W. T. Liu, S. Wu, *Nat. Nanotechnol.* **2014**, *9*, 825.

[69] C. Kim, I. Moon, D. Lee, M. S. Choi, F. Ahmed, S. Nam, Y. Cho, H. J. Shin, S. Park, W. J. Yoo, *ACS Nano* **2017**, *11*, 1588.

[70] L. Liang, Z. Shi, X. Tan, S. Sun, M. Chen, D. Dastan, B. Dong, L. Cao, *Adv. Mater.*

Interfaces **2022**, *9*, 1.

[71] Y. Hattori, T. Taniguchi, K. Watanabe, K. Nagashio, *ACS Appl. Mater. Interfaces* **2016**, *8*, 27877.

[72] A. Ranjan, N. Raghavan, M. Holwill, K. Watanabe, T. Taniguchi, K. S. Novoselov, K. L. Pey, S. J. O'Shea, *ACS Appl. Electron. Mater.* **2021**, *3*, 3547.

[73] J. K. Huang, Y. Wan, J. Shi, J. Zhang, Z. Wang, W. Wang, N. Yang, Y. Liu, C. H. Lin, X. Guan, L. Hu, Z. L. Yang, B. C. Huang, Y. P. Chiu, J. Yang, V. Tung, D. Wang, K. Kalantar-Zadeh, T. Wu, X. Zu, L. Qiao, L. J. Li, S. Li, *Nature* **2022**, *605*, 262.

Figures

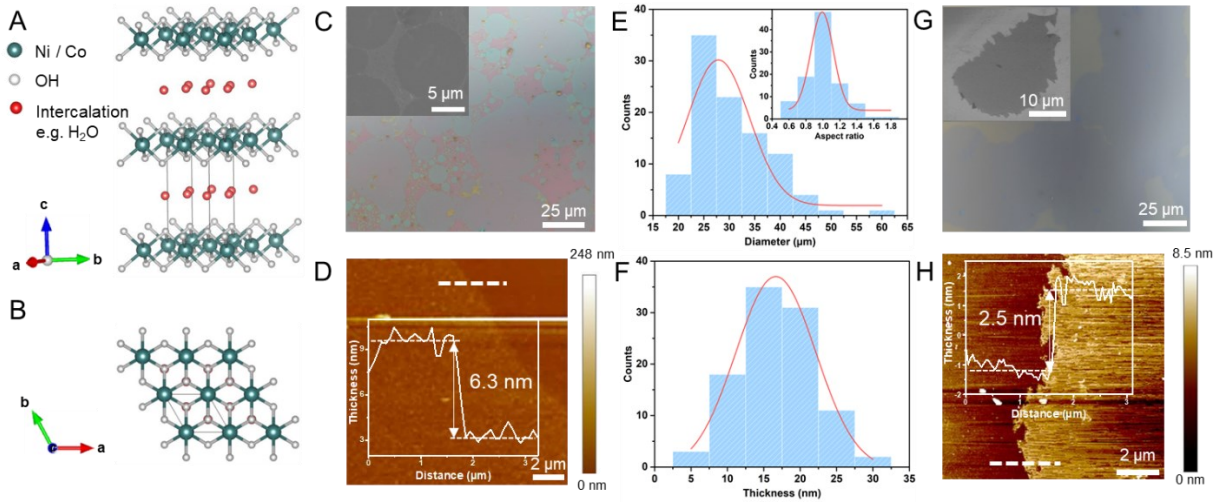

Fig. 1. Crystal structure and morphology characterization of M-$(OH)_2$, (M=Ni, Co) (A and **B)** Crystal structure of α-$M(OH)_2$. (**A**) Side view; (**B**) Top view. (**C**) Optical image and SEM image (inset) of synthesized $Ni(OH)_2$ flakes on SiO_2/Si substrate. (**D**) AFM image of a $Ni(OH)_2$ flake, the white dash line indicates the location where the thickness is measured. Inset: height profile along the white dash line. (**E**) Size distribution of 100 $Ni(OH)_2$ flakes in a randomly chosen area. Inset: aspect ratio distribution, which is defined as the ratio of diameters measured along two perpendicular directions, indicating the shape of flakes. (**F**) Thickness distribution of 100 $Ni(OH)_2$ flakes in a randomly chosen area. (**G**) Optical image of synthesized 2D $Co(OH)_2$ flakes on SiO_2/Si substrate, domain size reaches ~40 μm on one direction. Inset: SEM image of synthesized 2D $Co(OH)_2$ on SiO_2/Si substrate, showing the crystal domain is continuous. (**H**) AFM image of a $Co(OH)_2$ flake, the white dash line indicates the location where the thickness is measured. Inset: height profile along the white dash line, showing the thickness of the flakes is 2.5 nm.

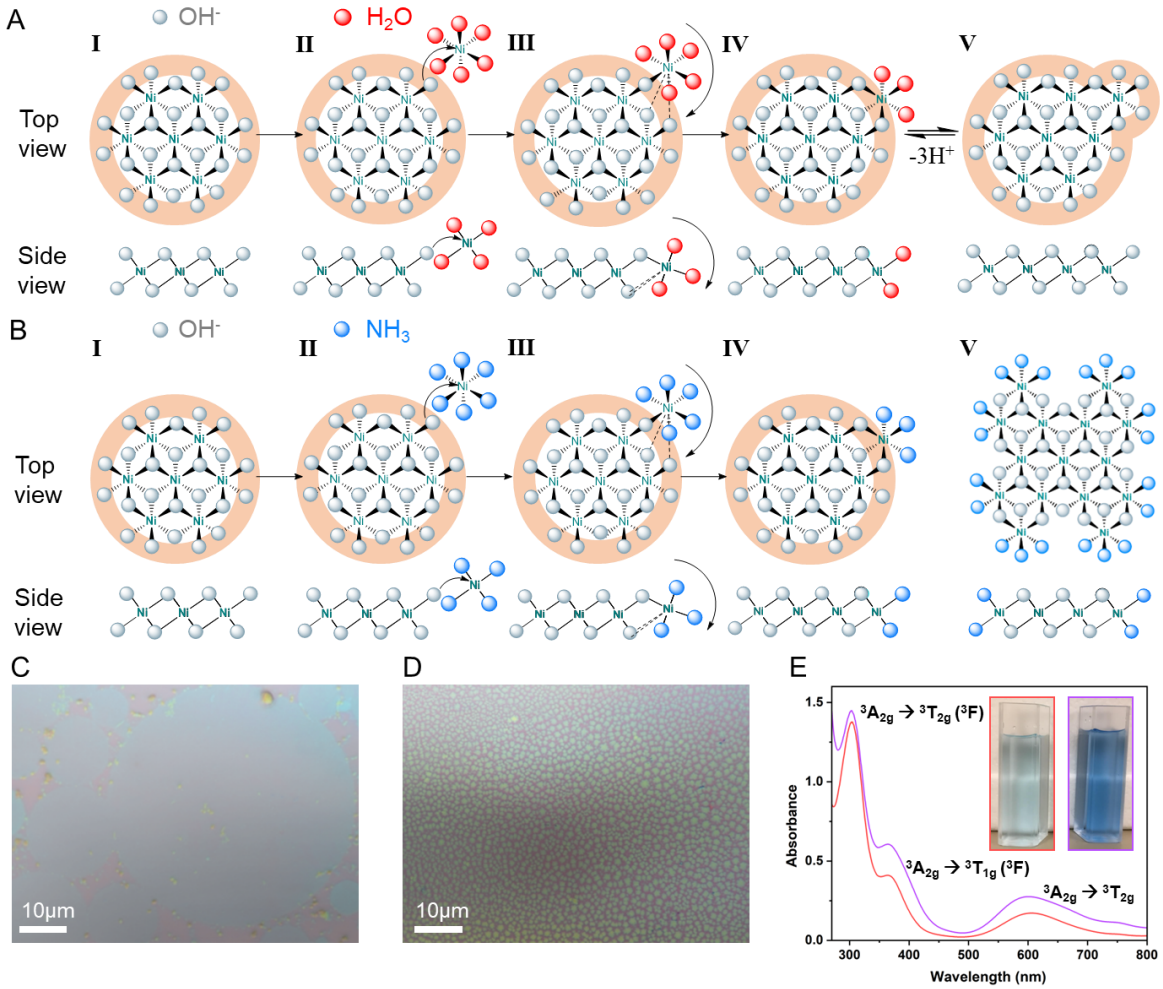

Fig. 2. 2D $Ni(OH)_2$ growth mechanism. (**A**) 2D growth mechanism of $Ni(OH)_2$ via edge-on condensation after nucleation. I. The buildup of localized negative charge (orange ring) incurred by edge OH^- ions on the nucleus attracts approach of Ni^{2+} ions; II. Ligand exchange at labile Ni^{2+} centers, undergoing substitution with hanging OH^- groups when proximal to an existing crystal, which guides continues substitution of terminal OH^- groups at newly bounded Ni^{2+}; III. The unit is locking into the crystal structure; IV. Deprotonation of coordinated H_2O or its displacement by OH^- to extend the crystal domain (V) or to continue the add-on (II). (**B**) Schematic of $[Ni(NH_3)_6]^{2+}$ blocking the growing nuclei and crystals, the orange ring represents the localized negative charge. (**C**) Optical image of the obtained 2D $Ni(OH)_2$ without additional NH_4OH, where circular flakes are widely observed. (**D**) Optical image of the obtained 2D $Ni(OH)_2$ with 0.6 ml additional NH_4OH, the crystal size are significantly decreased. (**E**) Absorbance of 2D $Ni(OH)_2/H_2O$ dispersion without (red curve) and with 0.6 ml additional NH_4OH (purple curve), three absorption bands assigned left to right as $^3A_{2g} \rightarrow {}^3T_{1g}$ (^3F), $^3A_{2g} \rightarrow {}^3T_{1g}$ (^3F), $^3A_{2g} \rightarrow {}^3T_{2g}$, consistent with homoleptic six-coordinate Ni(II) complexes. Inset: 2D $Ni(OH)_2/H_2O$ dispersion of (**C**) (left) and (**D**) (right).

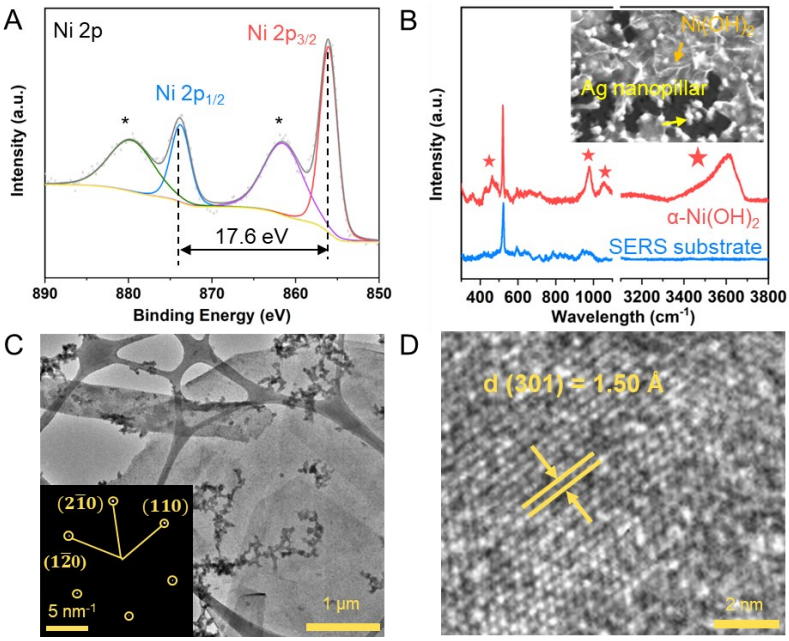

Fig. 3. Crystallographic characterization of $Ni(OH)_2$. (**A**) XPS spectra of Ni 2p, suggesting a 17.6 eV spin energy separation, which is characteristic of the Ni^{2+} in $Ni(OH)_2$. (**B**) Raman spectra of Ag nanopillar SERS substrate with and without $Ni(OH)_2$ thin flakes on. Characteristic peaks of α-$Ni(OH)_2$ indicated by "stars" are observed and a fingerprint one is observed at 3610 cm^{-1}. Inset: SEM image of Ag nanopillar SERS substrate with and without $Ni(OH)_2$ thin flakes on. (**C**) Low-magnification TEM image. Inset: the SAED pattern. (**D**) High-magnification TEM image, the d-spacing of (301) lattice plane is measured as 1.50 Å.

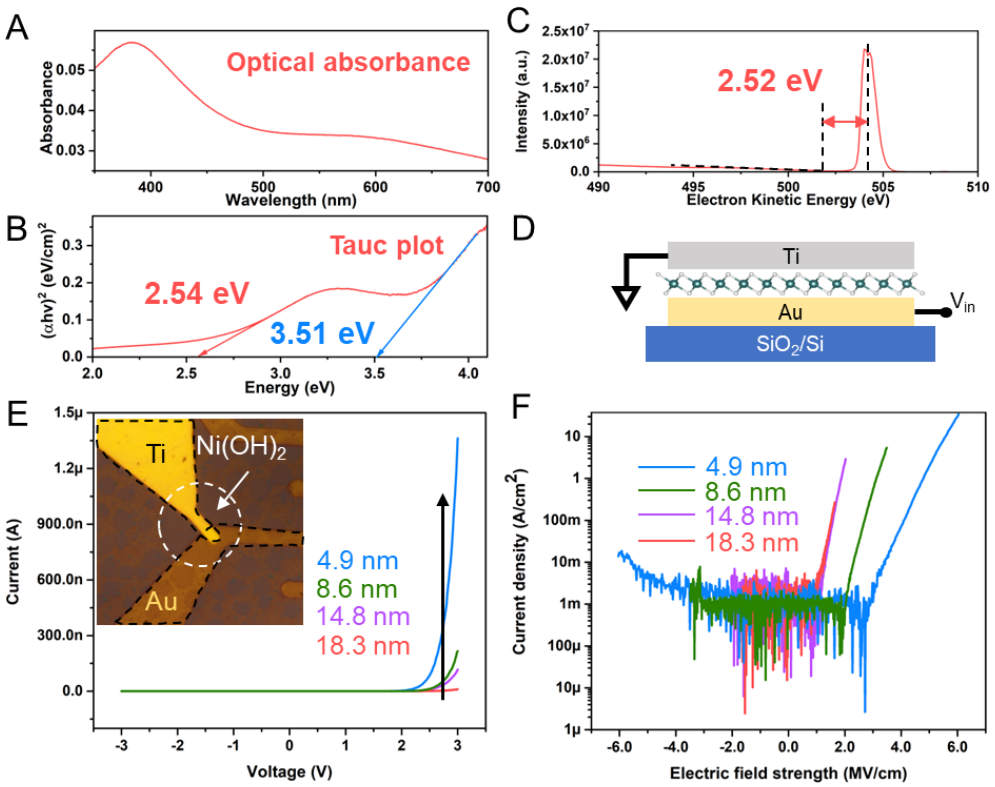

Fig. 4. Optical and electrical characterizations of $Ni(OH)_2$. (**A**) Optical absorption spectrum of few layers α-$Ni(OH)_2$ thin flakes on ITO glass, measured by UV-Vis from 300 nm to 700 nm. (**B**) Tauc plot derived from (A), the extrapolated bandgaps are 2.54 eV and 3.51 eV, corresponding to few layers and bulk α-$Ni(OH)_2$. (**C**) Band gap extrapolated from reflected electrons energy loss spectroscopy (REELS) by measuring the gap between the center of elastic scattering peak and the cutoff of the low energy loss peak is 2.52 eV. (**D**) Schematic of Au-$Ni(OH)_2$-Ti sandwich-like device. The top Ti electrode is grounded and voltage is applied on the bottom Au electrode for all measurements. (**E**) Typical I-V characteristics of samples with different thicknesses, from 4.9 nm to 18.3 nm. Current increases exponentially under positive bias on all four measured samples. Inset: optical image of the device. (**F**) Current density-electric field strength correlation of the tested samples with current in logarithm scale. The thinnest sample, 4.9 nm, exhibits the highest breakdown field, 4.47 MV/cm, which is comparable with commonly used dielectric layers.